46th AIAA/ASME/SAE/ASEE Joint Propulsion Conference & Exhibit
25 - 28 July 2010, Nashville, TN

AIAA 2010-6764

On the Viscous Bidirectional Vortex. Part 2: Nonlinear Beltramian Motion

Joshua W. Batterson* and Joseph Majdalani†
University of Tennessee Space Institute, Tullahoma, TN 37388, USA

In studying the inviscid bidirectional motion in a confined, cylindrical chamber, the Bragg-Hawthorne equation may be used as a starting point to obtain both linear and nonlinear models of the Stokes streamfunction under steady, incompressible, axisymmetric conditions. This article focuses on the axially nonlinear model that allows for slippage at the sidewall and a core singularity along its axis of rotation (see Majdalani, J., "Exact Eulerian Solutions of the Cylindrical Bidirectional Vortex," AIAA Paper 2009-5307, Denver, Colorado, Aug. 2009). Using the principles of matched-asymptotic expansion theory, the presence of viscous stresses in the forced vortex core are accounted for, thus leading to a composite-inner approximation for the tangential velocity that remains bounded along the centerline. Then through a boundary layer treatment of the wall region, the vanishing velocity requirement along the chamber's circumference is secured. Both wall and inner core layers are subsequently combined with the inviscid outer model into one, uniformly valid, tangential velocity formulation. A similar wall treatment involving dependent-variable transformations is repeated in the axial and radial directions to the extent of producing a composite expression for the total velocity field. Given a uniformly valid approximation for the velocity, characteristic flow features are readily derived including the wall and core boundary layers, pressure and vorticity distributions, and maximum velocity amplitudes and pressure gradients. These are compared to their counterparts arising in the analysis of the linear Beltramian solution. When averaged over the length of the chamber, the nonlinear axial dependence is seen to induce similar velocities and boundary layers to its linear counterpart, with the differences being in its appreciably reduced pressure dependence on the axial coordinate and substantially mollified leakage rate near the tangential injection site between the upward-moving annular fluid and the down-flow.

Nomenclature

A_i	=	inlet area
B	=	tangential angular momentum, ru_θ
H	=	total stagnation pressure head, $p + \frac{1}{2}u^2$
Q_i	=	nondimensional volumetric flow rate, $\bar{Q}_i/(Ua^2)$
Re	=	injection Reynolds number, $Ua/\nu = 1/\varepsilon$
S	=	swirl number, $\pi ab/A_i = \pi\beta\sigma$
U	=	average inflow velocity in the tangential direction, $\bar{u}_\theta(a, L)$
V	=	vortex Reynolds number, $Q_i Re(a/L) = (\varepsilon\sigma l)^{-1} = 2\pi\kappa/\varepsilon$
$\bar{Q}_i$	=	inlet volumetric flow rate
$\boldsymbol{u}$	=	nondimensional velocity, $(\bar{u}_r, \bar{u}_\theta, \bar{u}_z)/U$
a	=	chamber radius
b	=	chamber outlet radius
l	=	chamber aspect ratio, L/a
p	=	nondimensional pressure, $\bar{p}/(\rho U^2)$
r, z	=	nondimensional radial and axial coordinates, $(\bar{r}, \bar{z})/a$
s	=	scaled radial coordinate

Subscripts

0	=	reference value at the chamber headwall
θ	=	tangential component
c	=	represents a solution in the core
i	=	inlet property

*Graduate Research Assistant, Mechanical, Aerospace and Biomedical Engineering Department. Student Member AIAA.
†H. H. Arnold Chair of Excellence in Advanced Propulsion, Mechanical, Aerospace and Biomedical Engineering Department. Senior Member AIAA. Fellow ASME.

Copyright © 2010 by J. W. Batterson and J. Majdalani. Published by the American Institute of Aeronautics and Astronautics, Inc., with permission.

m = mode number
r = radial component
w = represents a solution near the wall
z = axial component

Symbols

α = constant, $\frac{\lambda_0}{2\beta J_1(\lambda_0\beta)}\left(\frac{1}{8}\lambda_0^2 - 1\right)$
β = normalized outlet radius, b/a
δ = characteristic boundary layer thickness
δ_p = location of maximum pressure gradient
ϵ = viscous parameter, $1/Re = \nu/(Ua)$
γ = constant, $\frac{\lambda_0}{4\beta J_1(\lambda_0\beta)}$
κ = inflow parameter, $Q_i/(2\pi l) = (2\pi\sigma l)^{-1}$
λ = eigenvalue
ν = kinematic viscosity
ω_f = constant angular speed of the forced vortex
$\boldsymbol{\omega}$ = vorticity vector
ψ = streamfunction
ρ = density
σ = modified swirl number, $Q_i^{-1} = S/(\pi\beta)$
υ = separation constant

Superscripts

$\bar{}$ = overbars denote a dimensional variable
c = denotes a composite solution
ci = denotes a composite-inner solution
i = denotes an inner solution
o = denotes an outer solution
w = denotes a near-wall solution

I. Introduction

Modeling bidirectional motions is of interest to a variety of applications including those in propulsion where the unique kinematic features associated with a cyclone can be leveraged in the design of so-called vortex-fired hybrid [1,2] and liquid rocket engines. [3] In this context, a self-reversing spiraling motion is induced in a combustion chamber through the tangential injection of an oxidizer fluid, liquid or gaseous. The elevated mixing rates and swirling intensities that accompany the formation of helical flows are thus exploited to improve combustion efficiency, increase the effective chamber length, and promote wall cooling. Reduction of wall heat transfer is also implemented by Matveev and Serbin [4] in the design of an innovative reverse-vortex (RV) plasma reactor that is shown to increase plasma generator efficiency. Related experiments and computational studies by Matveev *et al.* [5,6] confirm the confinement of high temperature regions to the core of their 'triple vortex.' In fact, their so-called Tornado Combustor shares similar features to the Vortex Combustion Cold-Wall Chamber (VCCWC) developed by Chiaverini *et al.* [3]

To numerically model the VCCWC flowfield, preliminary studies by Fang, Majdalani and Chiaverini [7,8] have been undertaken with the aim of characterizing the observed cyclonic motion under both cold and reactive flow conditions. Their computational work followed the theoretical development of the first exact solution of the bidirectional vortex by Vyas and Majdalani. [9] This complex-lamellar model corresponded to an inviscid, incompressible, cold-flow formulation of the problem in a confined cylindrical geometry. With some effort, it was extended to spherical geometry by Majdalani and Rienstra [10] who demonstrated the existence of additional solutions. The velocity profiles obtained thus far were derived from Euler's equations and displayed, as such, a singularity in their tangential component that led to unbounded behavior at the centerline. The singularity could be connected to the inability of swirl-dominated flows in satisfying the forced vortex requirement along their axis of rotation in a frictionless environment. [11,12]

To overcome the singularity in the tangential speed, Majdalani and Chiaverini [13] reconstructed the problem by starting with the Navier-Stokes equations and using suitable scaling laws to simplify the resulting framework. Then using matched-asymptotic expansions and the reciprocal of the Reynolds number as a small parameter, they managed

to obtain a uniformly valid approximation for the swirl velocity in which the viscous-dominated forced vortex core and wall boundary layers could be incorporated. Shortly thereafter, Batterson and Majdalani [14] completed the analysis by restoring wall friction and circumventing slippage in the remaining axial and radial directions. In the interim, a piecewise, constant shear stress model for the core region was advanced by Maicke and Majdalani. [15] Despite the fundamental dissimilarities in their formulations, the Batterson-Majdalani and Maicke-Majdalani models provided singularity-free representations of the original, complex-lamellar solution.

Guided by experimental evidence that suggests the possibility of dual solutions in cyclone separators, [16,17] Majdalani [18] resorted to the Bragg-Hawthorne equation to derive additional Beltramian and Trkalian models for the problem at hand. Among the newly obtained flowfields, two particular profiles displayed either linear or nonlinear axial dependence. Both were exact inviscid solutions that bore the characteristic singularity ascribed to axisymmetric, swirl-dominated, frictionless motion. While the first installment of this work concentrated on the linear solution, it is the purpose of this sequel to apply a similar viscous analysis to the nonlinear Beltramian field. As before, the relevant boundary layer equations will be obtained through the systematic truncation of the Navier-Stokes equations according to Prandtl's order of magnitude reduction approach. [14,19] Several further simplifications will be implemented with the aim of decoupling the boundary layer equations and turning them into ordinary differential equations. These will be solved asymptotically and the resulting approximations will be shown to be congruent with the endpoint requirements that restrict the swirl velocity at the centerline and the three-component velocity at the sidewall.

II. Formulation

The formulation of the nonlinear Beltramian problem follows the procedure that was first introduced in an article by Majdalani [18] and later revisited in the companion paper by Batterson and Majdalani. [20]

A. The Bragg-Hawthorne Equation

Using the same nomenclature and geometry as before, we recognize that the Bragg-Hawthorne equation for steady, inviscid, incompressible and axisymmetric motion may be written as

$$\frac{\partial^2\psi}{\partial r^2}-\frac{1}{r}\frac{\partial\psi}{\partial r}+\frac{\partial^2\psi}{\partial z^2}=r^2\frac{\mathrm{d}H}{\mathrm{d}\psi}-B\frac{\mathrm{d}B}{\mathrm{d}\psi} \tag{1}$$

where the tangential angular momentum B may be taken as $ru_\theta=\sqrt{C_m^2\psi^2+B_1}$, and the total pressure head may be assumed to be constant along streamlines where $\mathrm{d}H/\mathrm{d}\psi=0$. Under these auspices, we have

$$\frac{\partial^2\psi}{\partial r^2}-\frac{1}{r}\frac{\partial\psi}{\partial r}+\frac{\partial^2\psi}{\partial z^2}+C_m^2\psi=0 \tag{2}$$

One may recall that Eq. (2) is similar to the form employed by Culick [21] or Vyas and Majdalani [9] with the exception of an r^2 multiplying its last member. Being linear, we substitute $\psi=f(r)g(z)$ to obtain

$$-\frac{\ddot{g}}{g}=\frac{1}{f}\left(f''-\frac{1}{r}f'+C_m^2 f\right)=\begin{cases}0\\+\upsilon^2\\-\upsilon^2\end{cases} \tag{3}$$

The right-hand-side comprises three possible separation constants. The first leads to a linear axial dependence that is pursued by the authors in Part 1 of this paper series. [20] The second constant leads to a nonlinear, harmonic axial dependence that will be shortly presented and discussed.

B. The Nonlinear Beltramian Solution

For υ positive definite, a harmonic axial dependence emerges in the solution of $g(z)$. We get

$$g(r)=C_1\sin(\upsilon z)+C_2\cos(\upsilon z) \tag{4}$$

As for the radial equation, we obtain a simplified form of Bessel's equation,

$$f(r)=r\left[C_3J_1\left(r\sqrt{C_m^2-\upsilon^2}\right)+C_4Y_1\left(r\sqrt{C_m^2-\upsilon^2}\right)\right] \tag{5}$$

The general solution of Eq. (2) may hence be constructed from the product of $f(r)$ and $g(z)$, namely,

$$\psi = r\left[C_1 \sin(\upsilon z) + C_2 \cos(\upsilon z)\right]\left[C_3 J_1\left(r\sqrt{C_m^2 - \upsilon^2}\right) + C_4 Y_1\left(r\sqrt{C_m^2 - \upsilon^2}\right)\right]; \quad C_m^2 > \upsilon^2 \tag{6}$$

Next we apply physically appropriate boundary conditions.

1. Boundary Conditions

For an ideal vortex in a confined cylinder, one may impose

$$z = 0; \quad u_z(r,0) = 0 \quad \text{or} \quad \frac{1}{r}\frac{\partial\psi(r,0)}{\partial r} = 0 \tag{7a}$$

$$r = 0; \quad u_r(0,z) = 0 \quad \text{or} \quad -\frac{1}{r}\frac{\partial\psi(0,z)}{\partial z} = 0 \tag{7b}$$

$$r = 1; \quad u_r(1,z) = 0 \quad \text{or} \quad -\frac{1}{r}\frac{\partial\psi(1,z)}{\partial z} = 0 \tag{7c}$$

$$z = l; \quad Q_i = \int_0^{\beta}\int_0^{2\pi} \boldsymbol{u}\cdot\boldsymbol{n}\, r\,\mathrm{d}r = 2\pi\int_0^{\beta} u_z(r,l) r\,\mathrm{d}r = 2\pi\int_0^{\beta}\frac{1}{r}\frac{\partial\psi(r,l)}{\partial r}\, r\,\mathrm{d}r \tag{7d}$$

In the present case, one more condition is needed beyond the linear Beltramian model in order to properly determine the separation constant. The additional physical condition that we invoke takes into account the purely tangential velocity at $z = l$. Such a condition requires a vanishing radial component of the velocity at the endwall.

2. Exact Inviscid Solution

The first constraint in Eq. (7a) implies no injection at the headwall. From this condition two constants may be deduced, $C_2 = C_4 = 0$. Equation (6) becomes

$$\psi = \psi_0 \sin(\upsilon z) r J_1\left(r\sqrt{C_m^2 - \upsilon^2}\right); \quad \psi_0 = C_1 C_3 \tag{8}$$

The second constraint is concerned with axisymmetry and the prevention of crossflow along the centerline. This condition turns out to be tautological and, therefore, of no further benefit.

The third constraint implies the presence of a nontranspiring sidewall. This condition begets the eigenvalue equation, $J_1(\sqrt{C_m^2 - \upsilon^2}) = 0$, wherefrom $C_m^2 = {\lambda_m}^2 + \upsilon^2$ may be deduced, where λ_m are the roots of the Bessel function of the first kind. These are given by the standard sequence, $\lambda_m = \{3.83171, 7.01559, 10.1735, 13.3237, ...\}$. Realizing that solutions with $m \geq 1$ entail multiple flow reversals inside the chamber, we limit our analysis to the case of $\lambda_0 = 3.83171$ for which a single flow reversal occurs near the headwall. With the substitution of these constants, the streamfunction collapses into

$$\psi = \psi_0 \sin(\upsilon z)\, r J_1(\lambda_0 r); \quad C_0^2 > \upsilon^2 \tag{9}$$

Next, to determine the separation constant υ, we employ the auxiliary constraint that accompanies the assumption of tangential influx. By setting $u_r(r,l) = 0$ in the injection plane, we arrive at $\cos(\upsilon_j l) = 0$ whence $\upsilon_j = (j + \frac{1}{2})\pi/l$ may be retrieved. To preclude recirculation in the domain $z \leq l$, we solely consider the case of

$$\upsilon_j = \upsilon_0 = \frac{\pi}{2l}; \quad C_0^2 = \lambda_0^2 + \frac{\pi^2}{4l^2} \tag{10}$$

Other flow patterns associated with $j = 1, 2, 3...$ or $z > l$ will generate axially periodic vortex cells that do not correspond to the problem under investigation.

Lastly, we impose Eq. (7d) by requiring all incoming fluid to exit through the opening at the endwall. This enables us to calculate the last undetermined constant, $\psi_0 = Q_i/[2\pi\beta J_1(\lambda_0\beta)]$. At length, we collect[18]

$$\psi = \kappa l r \sin\left(\tfrac{1}{2}\pi z/l\right)\frac{J_1(\lambda_0 r)}{\beta J_1(\lambda_0\beta)}; \quad C_0^2 > \upsilon^2 \tag{11}$$

where $\kappa = Q_i/(2\pi l)$.

Recalling that $ru_\theta = \sqrt{C_0^2\psi^2 + B_1}$ and $u_\theta(1, l) = 1$, a straightforward expression may be obtained for the swirl velocity with $B_1 = 1$. The remaining components of velocity may be derived directly from ψ. We thus arrive at the normalized form of the nonlinear Beltramian profile,[18]

$$\begin{aligned}\boldsymbol{u} = &-\frac{\pi}{2}\kappa r\cos\left(\tfrac{1}{2}\pi z/l\right)\frac{J_1(\lambda_0 r)}{\beta J_1(\lambda_0\beta)}\,\boldsymbol{e}_r \\ &+ r^{-1}\sqrt{1+\frac{\kappa^2}{\beta^2 J_1^2(\lambda_0\beta)}\left(\lambda_0^2 l^2+\frac{1}{4}\pi^2\right)r^2\sin^2\left(\tfrac{1}{2}\pi z/l\right)J_1^2(\lambda_0 r)}\,\boldsymbol{e}_\theta \\ &+ \kappa l\lambda_0\sin\left(\tfrac{1}{2}\pi z/l\right)\frac{J_0(\lambda_0 r)}{\beta J_1(\lambda_0\beta)}\,\boldsymbol{e}_z \end{aligned} \tag{12}$$

III. Viscous Corrections

Recent studies by Majdalani and Chiaverini[13] and, later, Batterson and Majdalani[14] have adopted asymptotic avenues in seeking viscous corrections to the inviscid Eulerian solutions. In the companion paper,[20] these were applied to the treatment of the linear Beltramian motion. In what follows, a similar analysis will be undertaken for the purpose of characterizing the boundary layers of the nonlinear Beltramian solution.

A. Tangential Wall and Core Corrections

An order of magnitude reduction of the tangential momentum equation results in

$$\frac{u_r}{r}\frac{\partial}{\partial r}(ru_\theta) + u_z\frac{\partial u_\theta}{\partial z} = \varepsilon\left\{\frac{\partial}{\partial r}\left[\frac{1}{r}\frac{\partial}{\partial r}(ru_\theta)\right]\right\};\quad \varepsilon = \frac{\nu}{Ua} = Re^{-1} \tag{13}$$

Near the core, the inviscid solution smoothly approaches the axially invariant function r^{-1}. Similarly, $u_\theta \to 1$ at any axial position along the sidewall. This suggests that the boundary layer is essentially axially invariant. Majdalani and Chiaverini[13] used this observation to dismiss derivatives with respect to z. As before, this simplification enables us to reduce Eq. (13) into an ODE. Furthermore, we introduce $u_\theta = \xi_\theta(r)/r$ to the extent of producing

$$\varepsilon\left(\frac{\mathrm{d}^2\xi_\theta}{\mathrm{d}r^2} - \frac{1}{r}\frac{\mathrm{d}\xi_\theta}{\mathrm{d}r}\right) - u_r\frac{\mathrm{d}\xi_\theta}{\mathrm{d}r} = 0 \tag{14}$$

Then using u_r from the outer, inviscid solution, we obtain

$$\varepsilon\left(\frac{\mathrm{d}^2\xi_\theta}{\mathrm{d}r^2} - \frac{1}{r}\frac{\mathrm{d}\xi_\theta}{\mathrm{d}r}\right) + \frac{\pi\kappa J_1(\lambda_0 r)}{2\beta J_1(\lambda_0\beta)}\cos\left(\tfrac{1}{2}\pi z/l\right)\frac{\mathrm{d}\xi_\theta}{\mathrm{d}r} = 0 \tag{15}$$

The inclusion of u_r reintroduces the axial dependence into the governing equation. This behavior appears contrary to our original assumptions and must be handled carefully. It could be speculated that the core vortex in this case may be sensitive to variations in the crossflow velocity. Nonetheless, we also recall that, for an axisymmetric flowfield, continuity provides the link between the axial and radial velocities only. At the outset, u_θ can remain unaffected by an axially varying u_r. In order to make headway, we adopt an average value of the radial velocity in the core region by taking

$$(u_r)_{\text{avg}} = -\frac{\pi\kappa J_1(\lambda_0 r)}{2\beta J_1(\lambda_0\beta)}l^{-1}\int_0^l\cos\left(\tfrac{1}{2}\pi z/l\right) = -\frac{\kappa J_1(\lambda_0 r)}{\beta J_1(\lambda_0\beta)} \tag{16}$$

This leaves the governing equation as

$$\varepsilon\left(\frac{\mathrm{d}^2\xi_\theta}{\mathrm{d}r^2} - \frac{1}{r}\frac{\mathrm{d}\xi_\theta}{\mathrm{d}r}\right) + \frac{\kappa J_1(\lambda_0 r)}{\beta J_1(\lambda_0\beta)}\frac{\mathrm{d}\xi_\theta}{\mathrm{d}r} = 0 \tag{17}$$

Interestingly, Eq. (17) matches its counterpart in the linear Beltramian analysis.

1. Forced Core Vortex

Equation (17) is an applicable starting point for capturing either the viscous core or sidewall boundary layers. To this end, it is necessary to employ a stretched coordinate transformation and so we let $s = r/\delta$, where δ denotes the characteristic thickness of the boundary layer. Backward substitution into Eq. (17) leads to

$$\varepsilon\left(\frac{\mathrm{d}^2\xi_\theta^{(i)}}{\mathrm{d}s^2} - \frac{1}{s}\frac{\mathrm{d}\xi_\theta^{(i)}}{\mathrm{d}s}\right) + \kappa\delta\frac{J_1(\lambda_0\delta s)}{2\beta J_1(\lambda_0\beta)}\frac{\mathrm{d}\xi_\theta^{(i)}}{\mathrm{d}s} = 0 \tag{18}$$

where the superscript 'i' represents an 'inner' viscous solution. At this juncture, the boundary conditions may be prescribed to overcome the singularity at the centerline and to asymptotically approach the inviscid solution in the outer domain. These two conditions read

$$\begin{cases} \xi_\theta^{(i)}(0) = 0 \\ \lim\limits_{s\to\infty}\xi_\theta^{(i)} = \lim\limits_{r\to 0}\xi_\theta^{(o)} = 1 \end{cases} \tag{19}$$

where $\xi_\theta^{(o)} = ru_\theta^{(o)}$ represents the inviscid angular momentum in the tangential direction.

The characteristic boundary layer thickness, $\delta \sim \sqrt{\varepsilon/\kappa}$, is specified in a manner to produce equilibrium between diffusive and convective terms. With this distinguished limit, we recover

$$\frac{\mathrm{d}^2\xi_\theta^{(i)}}{\mathrm{d}s^2} + \left[\frac{\lambda_0 s}{2\beta J_1(\lambda_0\beta)} - \frac{1}{s}\right]\frac{\mathrm{d}\xi_\theta^{(i)}}{\mathrm{d}s} = 0 \tag{20}$$

By continuing with the leading-order expansion of the convective coefficient, we incur a minimal error for realistic values of ε and κ. The solution of Eq. (20) becomes

$$\xi_\theta^{(i)} = -\frac{2C_1\beta J_1(\lambda_0\beta)}{\lambda_0}\exp\left[-\frac{\lambda_0 s^2}{4\beta J_1(\lambda_0\beta)}\right] + C_2 \tag{21}$$

Subsequent application of $\xi_\theta^{(i)}(0) = 0$ gives

$$C_2 = \frac{2C_1\beta J_1(\lambda_0\beta)}{\lambda_0} \quad \text{or} \quad \xi_\theta^{(i)} = \frac{2C_1\beta J_1(\lambda_0\beta)}{\lambda_0}\left\{1 - \exp\left[-\frac{\lambda_0 s^2}{4\beta J_1(\lambda_0\beta)}\right]\right\} \tag{22}$$

The limit in Eq. (19) can also be applied to obtain

$$C_1 = \frac{\lambda_0}{2\beta J_1(\lambda_0\beta)} \quad \text{or} \quad \xi_\theta^{(i)} = 1 - \exp\left[-\frac{\lambda_0 s^2}{4\beta J_1(\lambda_0\beta)}\right] \tag{23}$$

A uniformly valid composite inner approximation follows, namely,

$$\xi_\theta^{(ci)} = \xi_\theta^{(o)} + \xi_\theta^{(i)} - \lim_{r\to 0}\xi_\theta^{(o)} \quad \text{or} \quad \xi_\theta^{(c)} = \left[1 + \frac{\kappa^2}{\beta^2 J_1^2(\lambda_0\beta)}\left(\lambda_0^2 l^2 + \frac{1}{4}\pi^2\right) r^2\sin^2\left(\tfrac{1}{2}\pi z/l\right) J_1^2(\lambda_0 r)\right]^{1/2} - \exp\left[-\frac{\kappa\lambda_0 r^2}{4\varepsilon\beta J_1(\lambda_0\beta)}\right] \tag{24}$$

In terms of u_θ, this solution may be expressed as

$$u_\theta^{(ci)} = r^{-1}\left[1 + \frac{\kappa^2}{\beta^2 J_1^2(\lambda_0\beta)}\left(\lambda_0^2 l^2 + \frac{1}{4}\pi^2\right) r^2\sin^2\left(\tfrac{1}{2}\pi z/l\right) J_1^2(\lambda_0 r) + 1\right]^{1/2} - \exp\left(-\frac{V}{2\pi}\gamma r^2\right); \quad \gamma = \frac{\lambda_0}{4\beta J_1(\lambda_0\beta)} \tag{25}$$

Based on Eq. (25) the constant angular speed associated with solid-body-rotation of the core vortex may be retrieved. Assuming $u_\theta^{(ci)} = \omega_f r$ in the core region, an expansion of Eq. (25) near $r = 0$ renders

$$u_\theta^{(ci)} = \frac{V}{8\pi\beta J_1(\beta\lambda_0)}\lambda_0 r + \frac{-V^2 + 4\pi^2\kappa^2\left(\pi^2 + 4l^2\lambda_0^2\right)\sin\left(\frac{1}{2}\pi z/l\right)^2}{128\pi^2\beta^2 J_1(\beta\lambda_0)^2}\lambda_0^2 r^3 + O(r^5) \tag{26}$$

Hence, in the vicinity of the centerline, fluid rotation occurs according to

$$\omega_f = \frac{V\lambda_0}{8\pi\beta J_1(\lambda_0\beta)} \approx 0.467919V \tag{27}$$

This result for ω_f is identical to its counterpart in the linear Beltramian case, both of which appearing at nearly twice the $\frac{1}{4}V$ value encountered in the complex-lamellar analysis.[13]

2. Sidewall Boundary Layer

Sidewall layers are also soluble from Eq. (17). To explore the endpoint boundary, we use $s = (1 - r)/\delta$ and transform the governing equation into

$$\varepsilon\left[\frac{\mathrm{d}^2\xi_\theta^{(i)}}{\mathrm{d}s^2} + \frac{\delta}{(1-s\delta)}\frac{\mathrm{d}\xi_\theta^{(i)}}{\mathrm{d}s}\right] - \kappa\delta\frac{J_1\left[\lambda_0(1-s\delta)\right]}{\beta J_1(\lambda_0\beta)}\frac{\mathrm{d}\xi_\theta^{(i)}}{\mathrm{d}s} = 0 \tag{28}$$

The nonlinear convective coefficient is further expanded by putting

$$J_1(\lambda_0 x) \approx \frac{\lambda_0 x}{2} - \frac{\lambda_0^3 x^3}{16} \approx -\frac{\lambda_0}{2}\left(\frac{\lambda_0^2}{8} - 1\right) + O(\delta); \quad x = (1 - \delta s) \tag{29}$$

Then using $\delta \sim \varepsilon/\kappa$, we arrive at

$$\frac{\mathrm{d}^2\xi_\theta^{(i)}}{\mathrm{d}s^2} + \alpha\frac{\mathrm{d}\xi_\theta^{(i)}}{\mathrm{d}s} = 0; \qquad \alpha = \frac{\lambda_0}{2\beta J_1(\lambda_0\beta)}\left(\frac{\lambda_0^2}{8} - 1\right) \tag{30}$$

where curvature terms are found to be of higher order. We find the solution of Eq. (30) to be

$$\xi_\theta^{(i)} = C_2 - \frac{C_1}{\alpha}e^{-\alpha s} \tag{31}$$

At this juncture, boundary conditions similar to those in the core can be defined along the wall. These consist of the no-slip at the wall and smooth blending with the outer solution. Mathematically, they can be written as

$$\begin{cases} \xi_\theta^{(i)}(0) = 0 \\ \lim\limits_{s\to\infty}\xi_\theta^{(i)}(s) = \lim\limits_{r\to 1}\xi_\theta^{(o)}(r) = 1 \end{cases} \tag{32}$$

Because the core corrections have no influence on the sidewall, we match our near-wall approximation to the inviscid outer field, $\xi_\theta^{(o)}$. This assortment of conditions leads to

$$\xi_\theta^{(i)} = 1 - \exp\left[-\frac{\lambda_0}{2\beta J_1(\lambda_0\beta)}\left(\frac{\lambda_0^2}{8} - 1\right)s\right] \tag{33}$$

The total composite solution can now be reproduced. In terms of the original variables, we find

$$u_\theta^{(c)} = r^{-1}\left\{\left[1 + \frac{\kappa^2}{\beta^2 J_1^2(\lambda_0\beta)}\left(\lambda_0^2 l^2 + \frac{1}{4}\pi^2\right)r^2\sin^2\left(\tfrac{1}{2}\pi z/l\right)J_1^2(\lambda_0 r)\right]^{1/2} - \exp\left(-\frac{V}{2\pi}\gamma r^2\right) - \exp\left[-\frac{V}{2\pi}\alpha(1-r)\right]\right\} \tag{34}$$

The last two members of Eq. (34) represent the net viscous contributions from the core and wall regions.

B. Axial Wall Correction

Viscous corrections to the axial velocity are necessary to satisfy the no-slip condition at the sidewall. A similar procedure to that outlined for the tangential wall corrections is employed here as well. Prandtl's order of magnitude reduction approach enables us to simplify the axial momentum equation into

$$u_r\frac{\partial u_z}{\partial r} + u_z\frac{\partial u_z}{\partial z} = -\frac{\partial p}{\partial z} + \varepsilon\left(\frac{\partial^2 u_z}{\partial r^2} + \frac{1}{r}\frac{\partial u_z}{\partial r}\right) \tag{35}$$

In the previous study,[14] the resultant boundary layer was shown to be almost exclusively dictated by the swirl dominated motion and, hence, tangential boundary layer character. The same arguments apply here.

In Eq. (35), the convective term may be readily linearized by taking the inviscid radial velocity as a leading-order representation in the boundary layer. We find

$$\varepsilon\left(\frac{\partial^2 u_z}{\partial r^2} + \frac{1}{r}\frac{\partial u_z}{\partial r}\right) + \frac{\pi\kappa}{2\beta J_1(\lambda_0\beta)}\cos\left(\tfrac{1}{2}\pi z/l\right)J_1(\lambda_0 r)\frac{\partial u_z}{\partial r} = -\frac{l\pi\kappa^2\lambda_0^2\left[J_0^2(\lambda_0 r) + J_1^2(\lambda_0 r)\right]\sin(\pi z/l)}{4\beta^2 J_1^2(\lambda_0\beta)} \tag{36}$$

Then using $u_z = \xi_z(r)\sin(\frac{1}{2}\pi z/l)J_0(\lambda_0 r)$, a retentive expression is obtained, namely,

$$\varepsilon\left\{-\frac{\lambda_0^2}{2}\sin\left(\tfrac{1}{2}\pi z/l\right)\left[J_0\left(\lambda_0 r\right)-J_2\left(\lambda_0 r\right)\right]\xi_z - 2\sin\left(\tfrac{1}{2}\pi z/l\right)\lambda_0 J_1\left(\lambda_0 r\right)\frac{\partial \xi_z}{\partial r} + \sin\left(\tfrac{1}{2}\pi z/l\right)J_0\left(\lambda_0 r\right)\frac{\partial^2 \xi_z}{\partial r^2}\right.$$
$$\left. + \frac{1}{r}\left[-\sin\left(\tfrac{1}{2}\pi z/l\right)\lambda_0 J_1\left(\lambda_0 r\right)\xi_z + \sin\left(\tfrac{1}{2}\pi z/l\right)J_0\left(\lambda_0 r\right)\frac{\partial \xi_z}{\partial r}\right]\right\}$$
$$+\frac{\pi\kappa}{2\beta J_1\left(\lambda_0\beta\right)}\cos\left(\tfrac{1}{2}\pi z/l\right)J_1\left(\lambda_0 r\right)\left[-\sin\left(\tfrac{1}{2}\pi z/l\right)\lambda_0 J_1\left(\lambda_0 r\right)\xi_z + \sin\left(\tfrac{1}{2}\pi z/l\right)J_0\left(\lambda_0 r\right)\frac{\partial \xi_z}{\partial r}\right]$$
$$= -\frac{l\pi\kappa^2\lambda_0^2\left[J_0^2\left(\lambda_0 r\right)+J_1^2\left(\lambda_0 r\right)\right]}{4\beta^2 J_1^2\left(\lambda_0\beta\right)}\sin\left(\pi z/l\right) \quad (37)$$

At this juncture, it is helpful to let $x = (1-\delta s)$ and expand the Bessel functions into

$$\begin{cases} J_0\left(\lambda_0 x\right) & \approx 1-\frac{\lambda_0^2 x^2}{4} \approx -\left(\frac{\lambda_0^2}{4}-1\right); & J_1\left(\lambda_0 x\right) & \approx \frac{\lambda_0 x}{2}-\frac{\lambda_0^3 x^3}{16} \approx -\frac{\lambda_0}{2}\left(\frac{\lambda_0^2}{8}-1\right) \\ J_2\left(\lambda_0 x\right) & \approx \frac{\lambda_0^2 x^2}{8}-\frac{\lambda_0^4 x^4}{96} \approx -\frac{\lambda_0^2}{8}\left(\frac{\lambda_0^2}{12}-1\right); & J_3\left(\lambda_0 x\right) & \approx \frac{\lambda_0^3 x^3}{48}-\frac{\lambda_0^5 x^5}{768} \approx -\frac{\lambda_0^3}{48}\left(\frac{\lambda_0^2}{16}-1\right) \end{cases} \quad (38)$$

Backward substitution of these expressions returns the sidewall boundary layer equation in the axial direction, specifically

$$\frac{\mathrm{d}^2\xi_z^{(w)}}{\mathrm{d}s^2} + \alpha\frac{\mathrm{d}\xi_z^{(w)}}{\mathrm{d}s} = 0; \qquad \alpha = \frac{\lambda_0}{2\beta J_1\left(\lambda_0\beta\right)}\left(\frac{\lambda_0^2}{8}-1\right) \quad (39)$$

where the convective coefficient is averaged over the chamber length.

Equation (39) may be solved using the boundary conditions prescribed by Eq. (32) with $\xi_z^{(o)} = \lambda\kappa/[\beta J_1(\lambda\beta)]$. We get

$$\xi_z^{(w)} = \frac{\lambda_0\kappa l}{\beta J_1\left(\lambda_0\beta\right)}\left\{1-\exp\left[-\alpha s\right]\right\} \quad (40)$$

Finally, a uniformly valid axial velocity may be recovered from the composite grouping,

$$\xi_z^{(c)} = \xi_z^{(o)} + \xi_z^{(w)} - \lim_{s\to\infty}\xi_z^{(w)}(s) \quad (41)$$

whence

$$u_z^{(c)} = \frac{\lambda_0\kappa l}{\beta J_1\left(\lambda_0\beta\right)}\sin\left(\tfrac{1}{2}\pi z/l\right)J_0\left(\lambda_0 r\right)\left\{1-\exp\left[-\frac{\lambda_0 V}{4\pi\beta J_1\left(\lambda_0\beta\right)}\left(\frac{\lambda_0^2}{8}-1\right)(1-r)\right]\right\} \quad (42)$$

C. Radial Wall Correction

The same arguments used heretofore can be applied to the radial momentum equation. We find

$$\varepsilon\left(\frac{\partial^2 u_r}{\partial r^2}+\frac{1}{r}\frac{\partial u_r}{\partial r}-\frac{u_r}{r^2}\right) - u_r\frac{\partial u_r}{\partial r} + \frac{u_\theta^2}{r} = \frac{\partial p}{\partial r} \quad (43)$$

The right-hand-side may be replaced by the outer, inviscid pressure,

$$\frac{\partial p}{\partial r} = -u_r^{(o)}\frac{\partial u_r^{(o)}}{\partial r} + \frac{1}{r}\left(u_\theta^{(o)}\right)^2 =$$
$$-\frac{\pi^2\kappa^2\lambda_0 J_1\left(\lambda_0 r\right)\left[J_0\left(\lambda_0 r\right)-J_2\left(\lambda_0 r\right)\right]}{8\beta^2 J_1^2\left(\lambda_0\beta\right)}\cos^2\left(\tfrac{1}{2}\pi z/l\right) - \frac{\pi^2\kappa^2\lambda_0 J_0\left(\lambda_0 r\right)J_1\left(\lambda_0 r\right)}{4\beta^2 J_1^2\left(\lambda_0\beta\right)}\sin^2\left(\tfrac{1}{2}\pi z/l\right) + \frac{1}{r}\left(u_\theta^{(o)}\right)^2 \quad (44)$$

According to Prandtl's theory, p does not change radially across the boundary layer.[19] This hypothesis eliminates the pressure term immediately. The same result may be confirmed by substituting Eq. (44) into Eq. (43) such that

$$\varepsilon\left(\frac{\partial^2 u_r}{\partial r^2}+\frac{1}{r}\frac{\partial u_r}{\partial r}-\frac{u_r}{r^2}\right) + \frac{\pi\kappa}{2\beta J_1\left(\lambda_0\beta\right)}\cos\left(\tfrac{1}{2}\pi z/l\right)J_1\left(\lambda_0 r\right)\frac{\partial u_r}{\partial r} = O(\kappa^2) \quad (45)$$

At this stage, we realize that a matched-asymptotic approximation cannot be obtained without a dependent-variable transformation. We therefore set $u_r = \xi_r(r)J_1(\lambda_0 r)$ and convert the above expression into

$$\varepsilon\left(\frac{\lambda_0^2}{4}\left[-3J_1(\lambda_0 r)+J_3(\lambda_0 r)\right]\xi_r+\lambda_0\left[J_0(\lambda_0 r)-J_2(\lambda_0 r)\right]\xi_r'+J_1(\lambda_0 r)\,\xi_r''\right.$$
$$\left.+\frac{1}{r}\left\{\frac{\lambda_0}{2}\left[J_0(\lambda_0 r)-J_2(\lambda_0 r)\right]\xi_r+J_1(\lambda_0 r)\,\xi_r'\right\}-\frac{\xi_r J_1(\lambda_0 r)}{r^2}\right)$$
$$+\frac{\pi\kappa}{2\beta J_1(\lambda_0\beta)}\cos\left(\tfrac{1}{2}\pi z/l\right)J_1(\lambda_0 r)\left\{\frac{\lambda_0}{2}\left[J_0(\lambda_0 r)-J_2(\lambda_0 r)\right]\xi_r+J_1(\lambda_0 r)\,\xi_r'\right\}=O(\kappa^2) \tag{46}$$

Another coordinate transformation is warranted by the need to magnify the wall region. This is accomplished by letting $s = (1-r)/\delta$ and expanding Eq. (46). Then using $\delta \sim \varepsilon/\kappa$, the leading-order expansion of the radial momentum equation in the wall region may be produced viz.

$$\frac{\mathrm{d}^2\xi_r^{(w)}}{\mathrm{d}s^2}+\alpha\frac{\mathrm{d}\xi_r^{(w)}}{\mathrm{d}s}=0; \qquad \alpha=\frac{\lambda_0}{2\beta J_1(\lambda_0\beta)}\left(\frac{\lambda_0^2}{8}-1\right) \tag{47}$$

The boundary conditions are the same as those found in Eq. (32) with $\xi_r^{(o)} = -\kappa/[\beta J_1(\lambda_0\beta)]$. Solving Eq. (47) results in the inner wall approximation

$$\xi_r^{(w)} = -\frac{\pi\kappa}{2\beta J_1(\lambda_0\beta)}\left(1-e^{-\alpha s}\right) \tag{48}$$

The composite radial velocity can hence be deduced and expressed in terms of the original variables. One gets

$$u_r^{(c)} = -\frac{\pi\kappa}{2\beta J_1(\lambda_0\beta)}\cos\left(\tfrac{1}{2}\pi z/l\right)J_1(\lambda_0 r)\left\{1-\exp\left[-\frac{V}{2\pi}\alpha(1-r)\right]\right\} \tag{49}$$

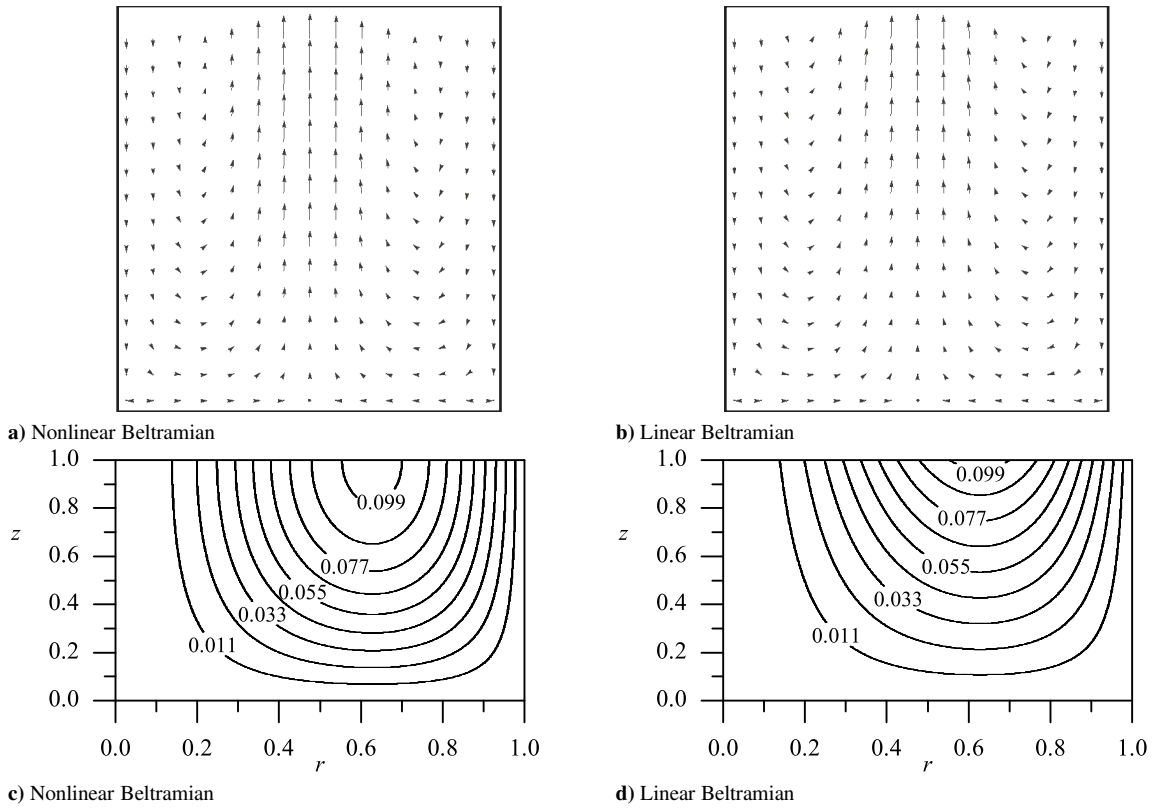

Figure 1. Vector (a,b) for l = 2 and streamline plots (c,d) of the nonlinear (left) and linear Beltramian models (right) for l = 1. Unless stated otherwise, we use κ= 0.103 everywhere.

IV. Results and Discussion

Vector and streamline plots of the linear and nonlinear Beltramian models are given side-by-side in Fig. 1. These plots display higher centerline velocities in the nonlinear case. Based on the vector directions, it may be inferred that a higher spillage rate occurs near the headwall of the chamber in the case of the nonlinear Beltramian motion. Such a flowfield may be advantageous in propulsive applications where the annular fluid consists of an oxidizer and where fuel is injected near the headwall at $z = 0$. The increased spillage near the headwall translates into higher combustion

Table 1. Comparison between the linear[20] and nonlinear Beltramian models

Linear Beltramian	$\alpha = \frac{\lambda_0}{2\beta J_1(\lambda_0\beta)}\left(\frac{1}{8}\lambda_0^2 - 1\right) \approx 4.91131$	$\gamma = \frac{\lambda_0}{4\beta J_1(\lambda_0\beta)} \approx 2.94002$
$u_r = -\frac{\kappa J_1(\lambda_0 r)}{\beta J_1(\lambda_0\beta)}\left[1 - e^{-\frac{V}{2\pi}\alpha(1-r)}\right] \approx -3.06915\kappa J_1(\lambda_0 r)\left[1 - e^{-\frac{V}{2\pi}\alpha(1-r)}\right]$		$(u_r)_{\max} \approx -1.78489\kappa$
$u_\theta = \frac{1}{r}\left\{\left[1 + \frac{\lambda_0^2\kappa^2 r^2 z^2 J_1^2(\lambda_0 r)}{\beta^2 J_1^2(\lambda_0\beta)}\right]^{1/2} - e^{-\frac{V}{2\pi}\gamma r^2} - e^{-\frac{V}{2\pi}\alpha(1-r)}\right\}$		$(u_\theta)_{\max} \approx \frac{\left\{1-\exp\left[\frac{1}{2}+\mathrm{pln}\left(-1,-\frac{1}{2\sqrt{e}}\right)\right]\right\}\sqrt{\lambda_0 V}}{2\sqrt{\pi\beta J_1(\beta\lambda_0)\left[-1-2\,\mathrm{pln}\left(-1,-\frac{1}{2\sqrt{e}}\right)\right]}}$
		$\approx 0.43654\sqrt{V}$
$u_z = \frac{\lambda_0\kappa z J_0(\lambda_0 r)}{\beta J_1(\lambda_0\beta)}\left[1 - e^{-\frac{V}{2\pi}\alpha(1-r)}\right] \approx 11.7601\kappa z J_0(\lambda_0 r)\left[1 - e^{-\frac{V}{2\pi}\alpha(1-r)}\right]$		$(u_z)_{\max} = 11.7601\kappa z$
$\delta_c \approx 2\sqrt{\frac{\pi\beta J_1(\beta\lambda_0)}{\lambda_0 V}\left[-1 - 2\,\mathrm{pln}\left(-1,-\frac{1}{2\sqrt{e}}\right)\right]} \approx \frac{1.63864}{\sqrt{V}}$		$\delta_w \approx \frac{2\pi}{V\alpha}\ln 100 \approx \frac{5.89153}{V}$
$\delta_i \approx \sqrt{\frac{\beta J_1(\lambda_0\beta)}{2\pi z^2\kappa^2\lambda_0^3}\left(\sqrt{V^2 + 32\pi^2 z^2\kappa^2\lambda_0^2\ln 100} - V\right)} \approx \frac{3.13716}{\sqrt{V}}$		
Nonlinear Beltramian	$\alpha = \frac{\lambda_0}{2\beta J_1(\lambda_0\beta)}\left(\frac{1}{8}\lambda_0^2 - 1\right) \approx 4.91131$	$\gamma = \frac{\lambda_0}{4\beta J_1(\lambda_0\beta)} \approx 2.94002$
$u_r = -\frac{\pi\kappa}{2\beta J_1(\lambda_0\beta)}\cos\left(\frac{1}{2}\pi z/l\right) J_1(\lambda_0 r)\left[1 - e^{-\frac{V}{2\pi}\alpha(1-r)}\right]$		$(u_r)_{\max} = -2.80518\kappa\cos\left(\frac{1}{2}\pi z/l\right)$
$\approx -4.82101\kappa\cos\left(\frac{1}{2}\pi z/l\right) J_1(\lambda_0 r)\left[1 - e^{-\frac{V}{2\pi}\alpha(1-r)}\right]$		
$u_\theta = r^{-1}\left\{\left[1 + \frac{\kappa^2}{\beta^2 J_1^2(\lambda_0\beta)}\left(\lambda_0^2 l^2 + \frac{1}{4}\pi^2\right) r^2 \sin^2\left(\frac{1}{2}\pi z/l\right) J_1^2(\lambda_0 r)\right]^{1/2}\right.$		$(u_\theta)_{\max} \approx \frac{\left\{1-\exp\left[\frac{1}{2}+\mathrm{pln}\left(-1,-\frac{1}{2\sqrt{e}}\right)\right]\right\}\sqrt{\lambda_0 V}}{2\sqrt{\pi\beta J_1(\beta\lambda_0)\left[-1-2\,\mathrm{pln}\left(-1,-\frac{1}{2\sqrt{e}}\right)\right]}}$
$\left. - e^{-\frac{V}{2\pi}\gamma r^2} - e^{-\frac{V}{2\pi}\alpha(1-r)}\right\}$		$\approx 0.43654\sqrt{V}$
$u_z = \frac{\lambda_0\kappa l}{\beta J_1(\lambda_0\beta)}\sin\left(\frac{1}{2}\pi z/l\right) J_0(\lambda_0 r)\left[1 - e^{-\frac{V}{2\pi}\alpha(1-r)}\right]$		$(u_z)_{\max} \approx 11.7601\kappa l\sin\left(\frac{1}{2}\pi z/l\right)$
$\approx 11.7601\kappa l\sin\left(\frac{1}{2}\pi z/l\right)\left[1 - e^{-\frac{V}{2\pi}\alpha(1-r)}\right]$		
$\delta_c \approx 2\sqrt{\frac{\pi\beta J_1(\beta\lambda_0)}{\lambda_0 V}\left[-1 - 2\,\mathrm{pln}\left(-1,-\frac{1}{2\sqrt{e}}\right)\right]} \approx \frac{1.63864}{\sqrt{V}}$		$\delta_w \approx \frac{2\pi}{V\alpha}\ln 100 \approx \frac{5.89153}{V}$
$\delta_i \approx \sqrt{\frac{2\beta J_1(\lambda_0\beta)}{\kappa^2\lambda_0\left(\pi^2+4l^2\lambda_0^2\right)}\csc^2\left(\frac{1}{2}\pi z/l\right)\left(\sqrt{V^2 + 4\pi^2\kappa^2\left(\pi^2 + 4l^2\lambda_0^2\right)[1-\cos(\pi z/l)]\ln 100} - V\right)} \approx \frac{3.13716}{\sqrt{V}}$		

efficiency and O/F ratios near the fuel injection site as well as reduced oxidizer leakage near the endwall where a nozzle is attached at $z = l$. For the readers convenience, a listing of the principal linear and nonlinear Beltramian parameters is provided in Table 1. Therein, it is clear that the boundary layers in both linear and nonlinear models are approximately the same, a conclusion that will be reached in the forthcoming analysis. This leaves differences in the inviscid solutions as the separating attributes between the two flowfields. These seem to translate into each of the boundary layer profiles during matching, albeit to a much lesser degree.

A. Tangential Velocity Distribution

The presence of a forced vortex suppresses the singularity at the centerline. This is accomplished by causing the core region to spin as a solid body with a tangential speed that is directly proportional to the radial distance from the centerline. Near the sidewall, a thin boundary layer is formed that is highly dependent on viscosity and injection characteristics.

In Fig. 2a, the swirl velocity is plotted at three different axial positions and one value of $V = 650$. Based on this graph, it is clear that u_θ varies ever so slightly with the axial position. The same behavior characterized previous models except for the complex-lamellar solution that remained strictly independent of the axial coordinate.[9] Yet when the vortex Reynolds number is increased from 200 to 800 at fixed $z = 1$, substantial variations in the velocity profile may be noted, as shown in Fig. 2b. These variations exceed those of the complex-lamellar profile and may lead to unrealistic values under turbulent conditions unless an effective vortex Reynolds number is used according to Maicke and Majdalani.[15] As usual, successive increases in V will give rise to a narrower forced vortex core as shown in Fig. 2b.

To estimate the maximum tangential velocity, it is sufficient to examine $u_\theta^{(ci)}$. Contributions due to sidewall corrections do not matter here. Then using $r = \delta_c$ for the edge of the core vortex, it may be shown that the z dependence may be dismissed to the extent of producing

$$\delta_c \approx 2\sqrt{\frac{\pi\beta J_1(\beta\lambda_0)}{\lambda_0 V}\left[-1-2\,\mathrm{pln}\left(-1,-\frac{1}{2\sqrt{e}}\right)\right]} \approx \frac{1.63864}{\sqrt{V}} \tag{50}$$

Interestingly, we find the characteristic radius of the forced vortex to be asymptotically equivalent for both linear and nonlinear Beltramian models. It amounts to nearly 73.1% of its value in the complex-lamellar case where $\delta_c \approx 2.2418/\sqrt{V}$. The two Beltramian solutions also achieve the same maximum swirl velocity,

$$(u_\theta)_{\max} \approx \frac{1-e^{\frac{1}{2}+\mathrm{pln}\left(-1,-\frac{1}{2\sqrt{e}}\right)}}{2\sqrt{\pi\beta J_1(\beta\lambda_0)\left[-1-2\,\mathrm{pln}\left(-1,-\frac{1}{2\sqrt{e}}\right)\right]}}\sqrt{\lambda_0 V} \approx 0.43654\sqrt{V} \tag{51}$$

This approximation incurs a less than 0.3% error when benchmarked against numerical root solving. Compared to the complex-lamellar profile, where u_θ peaks at $0.3191\sqrt{V}$, the speed ratio is $0.43654/0.3191 = 1.368$.

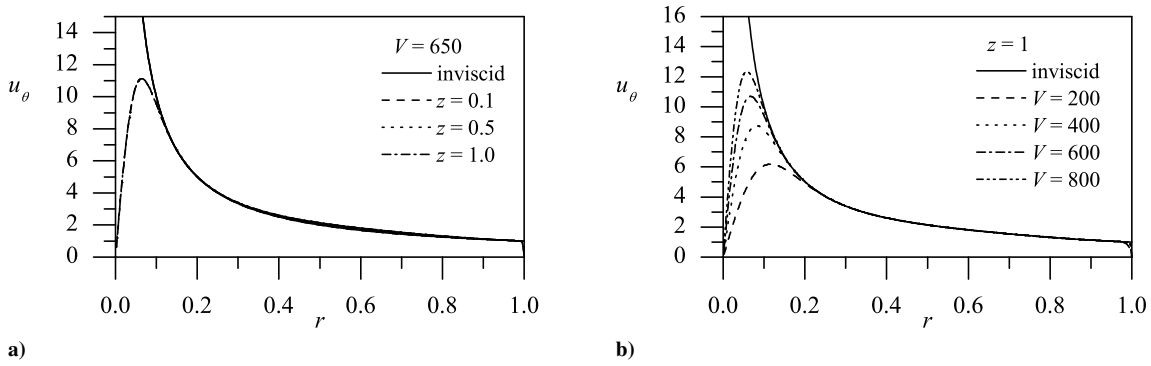

Figure 2. Tangential velocity plots showing effects of a) axial variations and b) sequentially increasing V. Here $\kappa = 0.103$ and $l = 1$ for all plots.

B. Axial Velocity Distribution

Figure 3a illustrates the nonlinear dependence of u_z on the axial position. The composite axial approximation is clearly capable of satisfying the velocity adherence requirement at $r = 1$. Upon closer scrutiny, it may be seen that the axial dependence of u_z is strictly an artifact of the inviscid formulation. To avoid recirculation, the model is confined to $0 \leq z \leq l$. The magnification in Fig. 3b serves to describe the sensitivity of the boundary layer on the vortex Reynolds number. The trends observed are consistent with those attributed to the linear Beltramian model. One can see from Fig. 3b that, as the vortex Reynolds number increases, the boundary layer thickness diminishes, and the solution approaches its inviscid representation. In fact, this observation may be readily confirmed by setting $V \longrightarrow \infty$ in Eq. (42) to the extent of recovering the inviscid solution.

Along the centerline, the maximum speed may be written as

$$(u_z)_{\max} = u_z(0,z) = \frac{\kappa l \lambda_0 J_0(0)}{\beta J_1(\lambda_0 \beta)} \sin\left(\tfrac{1}{2}\pi z/l\right)\left\{1 - \exp\left[-\frac{\lambda_0 V}{4\pi\beta J_1(\lambda_0\beta)}\left(\frac{\lambda_0^2}{8} - 1\right)\right]\right\} \approx 11.7601\kappa l \sin\left(\tfrac{1}{2}\pi z/l\right) \tag{52}$$

The peak value occurs at $z = l$ where Eq. (52) matches the linear Beltramian $(u_z)_{\max}$, both being 87.2% larger than the maximum centerline speed, $2\pi\kappa l$, associated with the complex-lamellar motion.[13]

C. Radial Velocity Distribution

Although we retain the exponential decay argument found in the tangential and axial boundary layers, the graphical representation of the radial velocity in Fig. 4a shows almost no axial sensitivity. The magnification in Fig. 4b illustrates, however, the smoothing effect caused by viscous stresses near the wall where both u_r and its derivative are compelled to vanish as $r \longrightarrow 1$. This effect is corroborated in the numerical work of Morgan,[22,23] Blasius,[24] and others.

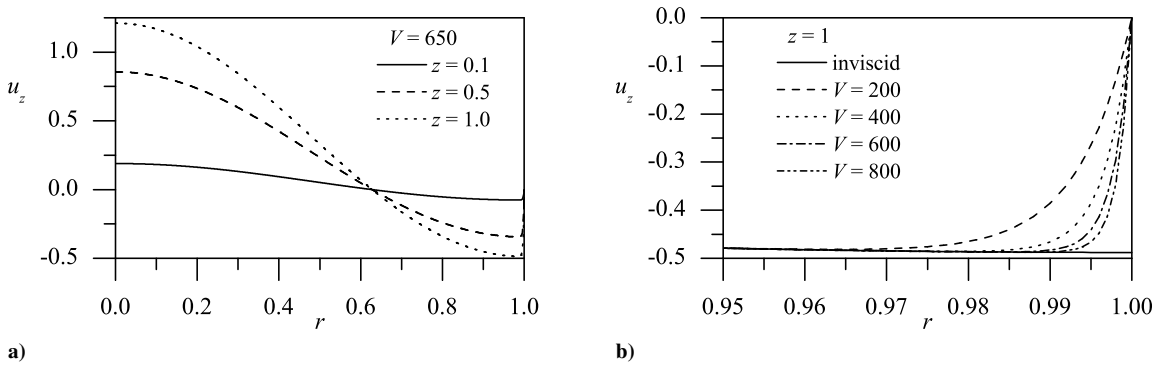

Figure 3. Axial velocity plots showing effects of a) axial variations and b) sequentially increasing V.

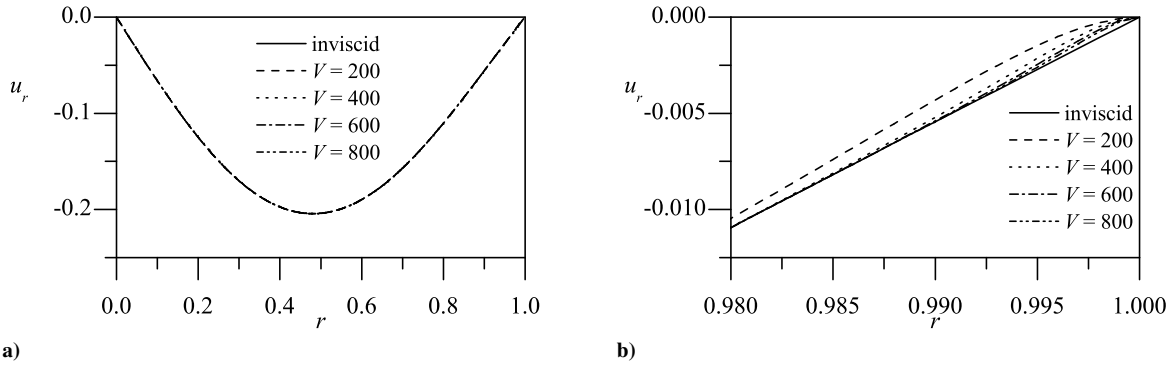

Figure 4. Variation of u_r with successive increases in V shown over a) the entire chamber radius and b) the thin viscous region.

D. Boundary Layer Thickness

Using Prandtl's convention, we take δ_i to be the boundary layer thickness that must be traversed in order to reach 99% of the outer solution. To determine the inner core thickness, δ_i, we may resort to Eq. (25) and extract the highly nonlinear expression

$$-\frac{V}{2\pi}\gamma r^2 = \ln\left\{\frac{1}{100}\left[1+\frac{\kappa^2}{\beta^2 J_1^2(\lambda_0\beta)}\left(\lambda_0^2 l^2+\frac{1}{4}\pi^2\right)r^2\sin^2\left(\tfrac{1}{2}\pi z/l\right)J_1^2(\lambda_0 r)\right]^{1/2}\right\} \tag{53}$$

Fortuitously, a one-term Taylor series expansion of the above leads to

$$\delta_i \approx \sqrt{\frac{2\beta J_1(\lambda_0\beta)}{\kappa^2\lambda_0\left(\pi^2+4l^2\lambda_0^2\right)}\csc^2\left(\tfrac{1}{2}\pi z/l\right)\left(-V+\sqrt{V^2+8\pi^2\kappa^2\left(\pi^2+4l^2\lambda_0^2\right)[1-\cos(\pi z/l)]\ln(10)}\right)}$$

$$\approx 4\sqrt{\frac{\pi\beta J_1(\lambda_0\beta)\ln 10}{\lambda_0 V}} \approx \frac{3.13716}{\sqrt{V}} \tag{54}$$

and so $\delta_i/\delta_c \approx 1.91449$. In Eq. (54), the present solution retains a small, albeit negligible, dependence on z. Based on the asymptotic treatment of the core, the edge of the boundary layer is reached at nearly twice the distance from the centerline to the locus of $(u_\theta)_{\max}$.

To describe the adjoining sidewall layer, δ_w, we evaluate the radius at which the solution regains 99% of the outer field. For the tangential velocity, the edge of the boundary layer is given by

$$-\frac{V}{2\pi}\alpha(1-r) = \ln\left\{\frac{1}{100}\left[1+\frac{\kappa^2}{\beta^2 J_1^2(\lambda_0\beta)}\left(\lambda_0^2 l^2+\frac{1}{4}\pi^2\right)r^2\sin^2\left(\tfrac{1}{2}\pi z/l\right)J_1^2(\lambda_0 r)\right]^{1/2}\right\} \tag{55}$$

The thickness of the wall region can be retrieved through the use of a one-term Taylor-series expansion of Eq. (55). We get

$$\delta_w = 1-r \approx \frac{2\pi}{V\alpha}\ln(100) \tag{56}$$

The approximation undertaken above renders the boundary layer thickness axially invariant. In practice, we find the maximum difference between Eq. (55) and Eq. (56) to be less than 0.2%. At the outset, we may require the viscous corrections in the axial and radial directions to conform to that of the tangential.[14] This realization leads to the same sidewall boundary layers in the axial and radial velocities. For the sake of comparison, we provide in Fig. 5 a plot of the three boundary layers along with $(u_\theta)_{\max}$ at fixed z. This graph is supplemented by Table 2 where typical values of δ_i and δ_w are posted at several axial positions and $V = 200, 400, \ldots, 1000$. From this table, it may be easily inferred that axial variations in the boundary layer are not only negligible but nearly identical to those connected with the linear Beltramian motion.

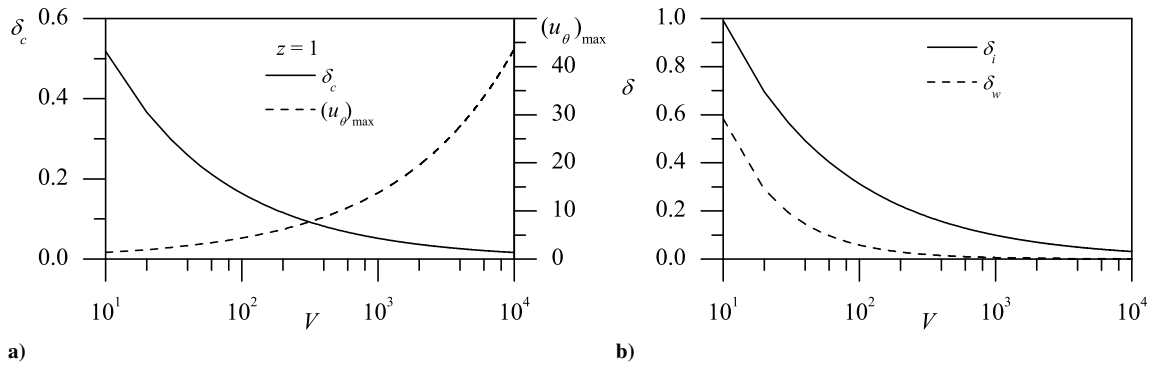

Figure 5. Effect of increasing V on a) the forced vortex core thickness δ_c with its peak tangential velocity, and b) Prandtl's inner core and sidewall boundary layers.

Table 2. Prandtl's inner core and sidewall boundary layer thicknesses at different positions and vortex Reynolds numbers

	Inner boundary layer, δ_i					Sidewall boundary layer, δ_w				
z	$V = 200$	$V = 400$	$V = 600$	$V = 800$	$V = 1000$	$V = 200$	$V = 400$	$V = 600$	$V = 800$	$V = 1000$
0	0.2218	0.1569	0.1281	0.1109	0.0992	0.0295	0.0147	0.0098	0.0074	0.0059
0.25	0.2218	0.1569	0.1281	0.1109	0.0992	0.0295	0.0147	0.0098	0.0074	0.0059
0.5	0.2218	0.1568	0.1281	0.1109	0.0992	0.0295	0.0147	0.0098	0.0074	0.0059
0.75	0.2217	0.1568	0.1281	0.1109	0.0992	0.0294	0.0147	0.0098	0.0074	0.0059
1	0.2217	0.1568	0.1281	0.1109	0.0992	0.0294	0.0147	0.0098	0.0074	0.0059

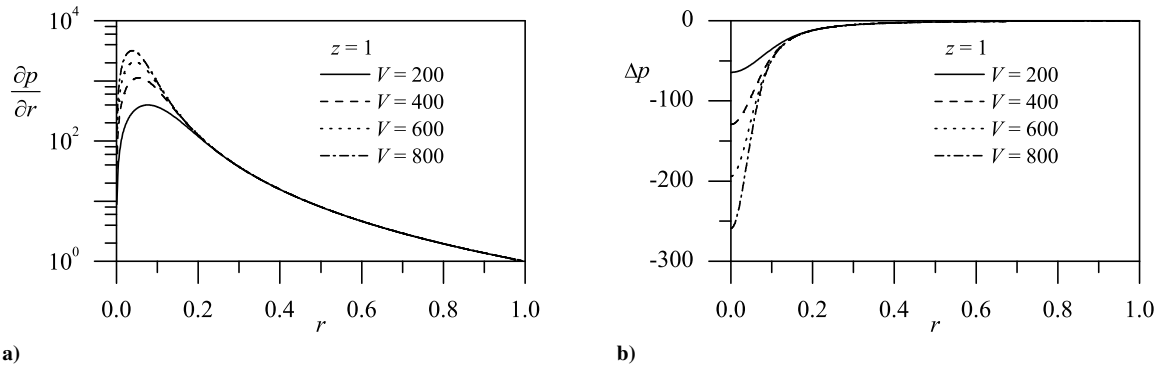

Figure 6. Variation of a) the radial pressure gradient and b) the pressure with successive increases in V.

E. Pressure Distribution

The right-hand-sides of Euler's radial and axial momentum equations readily produce the corresponding pressure gradients. For example, the radial component may be approximated by

$$\frac{\partial p}{\partial r} \approx \frac{1}{r^3}\left(e^{-\frac{V}{\pi}\alpha(1-r)} + e^{-\frac{V}{\pi}\gamma r^2} - 2e^{-\frac{V}{2\pi}\alpha(1-r)} + 2e^{-\frac{V}{2\pi}\gamma r^2}\right) \tag{57}$$

The above expression is illustrated in Fig. 6a where, unlike the linear Beltramian model, axially varying terms are ignored. This may be attributed to the solution being confined to $0 \le z \le l$ and $\sin(\frac{1}{2}\pi z/l)$ never exceeding unity. The bracketing of the sine term ensures that all axial contributions in the pressure remain transcendentally small, especially that they are further multiplied by κ^2. We can therefore write $\Delta p = p - p_0$, where $p_0 = p_0(1, 0)$ alludes to the normalized pressure at the corner of the headwall. Then by integrating Eq. (57), we collect

$$\begin{aligned}\Delta p\,(r,z) = {} & \frac{r^2-1}{2r^2} - \frac{V}{2\pi}\alpha + \frac{\pi^2 + \pi\alpha V - \alpha^2 V^2 \mathrm{Ei}\left(\frac{V}{\pi}\alpha\right)e^{-\frac{V}{\pi}\alpha}}{2\pi^2} \\ & - \frac{\pi\,(\pi + V\alpha r)\,e^{-\frac{V}{\pi}\alpha(1-r)} - r^2\alpha^2 V^2 \mathrm{Ei}\left(\frac{V}{\pi}\alpha r\right)e^{-\frac{V}{\pi}\alpha}}{2\pi^2 r^2} \\ & + \frac{1}{r^2}\left(e^{-\frac{V}{2\pi}\gamma r^2} - \frac{1}{2}e^{-\frac{V}{\pi}\gamma r^2}\right) + \frac{\pi}{2\pi}\left(e^{-\frac{V}{\pi}\gamma} - 2e^{-\frac{V}{2\pi}\gamma}\right) + \frac{V\gamma}{2\pi}\left[\mathrm{Ei}\left(-\frac{V}{\pi}\gamma\right) - \mathrm{Ei}\left(-\frac{V}{\pi}\gamma r^2\right)\right] \\ & + \frac{V\gamma}{2\pi}\left[\mathrm{Ei}\left(-\frac{V}{2\pi}\gamma r^2\right) - \mathrm{Ei}\left(-\frac{V}{2\pi}\gamma\right)\right] + \frac{\alpha^2 V^2}{4\pi^2}\mathrm{Ei}\left(\frac{V}{2\pi}\alpha\right)e^{-\frac{V}{2\pi}\alpha} \\ & + \frac{2\pi\,(2\pi + V\alpha r)\,e^{-\frac{V}{2\pi}\alpha(1-r)} - r^2\alpha^2 V^2 \mathrm{Ei}\left(\frac{V}{2\pi}\alpha r\right)e^{-\frac{V}{2\pi}\alpha}}{4r^2\pi^2}\end{aligned} \tag{58}$$

For realistically short chambers, it may be shown that the contribution of the axial pressure gradient to the total calculation of p remains several orders of magnitude smaller than its radial counterpart. As such, it may be reasonable to consider the pressure given by Eq. (58) to be representative of the total pressure profile. Figure 6b displays its

behavior, including the large characteristic pressure drop in the core region. The simulated vacuum around the axis of rotation gives rise to a negative radial crossflow that assists in drawing the fluid traveling in the annular portion of the chamber inwardly.

F. Vorticity Distribution

The vorticity profile can be calculated from

$$\boldsymbol{\omega} = \nabla \times \boldsymbol{u} = -\frac{\partial u_\theta}{\partial z}\boldsymbol{e}_r + \left(\frac{\partial u_r}{\partial z} - \frac{\partial u_z}{\partial r}\right)\boldsymbol{e}_\theta + \left(\frac{\partial u_\theta}{\partial r} + \frac{u_\theta}{r}\right)\boldsymbol{e}_z \tag{59}$$

With the inclusion of viscous corrections, we readily obtain

$$\begin{aligned}\boldsymbol{\omega} = &-\frac{\pi r\kappa^2\left(\frac{\pi^2}{4} + l^2\lambda_0{}^2\right)J_1{}^2(\lambda_0 r)}{4l\beta^2 J_1(\lambda_0\beta)\sqrt{1 + \frac{r^2\kappa^2\left(\frac{\pi^2}{4}+l^2\lambda_0{}^2\right)}{\beta^2 J_1(\lambda_0\beta)}\sin^2\left(\frac{\pi}{l}z\right)J_1{}^2(\lambda_0 r)}}\sin\left(\frac{\pi}{l}z\right)\boldsymbol{e}_r \\ &+ \frac{\kappa}{l\beta J_1(\lambda_0\beta)}\sin\left(\frac{\pi}{2l}z\right)\left\{\frac{Vl^2\alpha\lambda_0}{2\pi}J_0(\lambda_0 r)\,e^{-\frac{V}{2\pi}\alpha(1-r)} + \left(\frac{\pi^2}{4} + l^2\lambda_0{}^2\right)J_1(\lambda_0 r)\left(1 - e^{-\frac{V}{2\pi}\alpha(1-r)}\right)\right\}\boldsymbol{e}_\theta \\ &+ \left\{\frac{V}{2\pi}\left(2\gamma e^{-\frac{V}{2\pi}\gamma r^2} - r^{-1}\alpha e^{-\frac{V}{2\pi}\alpha(1-r)}\right) + \frac{r\kappa^2\lambda_0 J_0(\lambda_0 r)J_1(\lambda_0 r)\left(\frac{\pi^2}{4} + l^2\lambda_0{}^2\right)\left[1 - \cos\left(\frac{\pi}{l}z\right)\right]}{4\beta^2 J_1^2(\lambda_0\beta)\sqrt{1 + \frac{r^2\kappa^2\left(\frac{\pi^2}{4}+l^2\lambda_0{}^2\right)}{\beta^2 J_1(\lambda_0\beta)}\sin^2\left(\frac{\pi}{l}z\right)J_1{}^2(\lambda_0 r)}}\right\}\boldsymbol{e}_z\end{aligned} \tag{60}$$

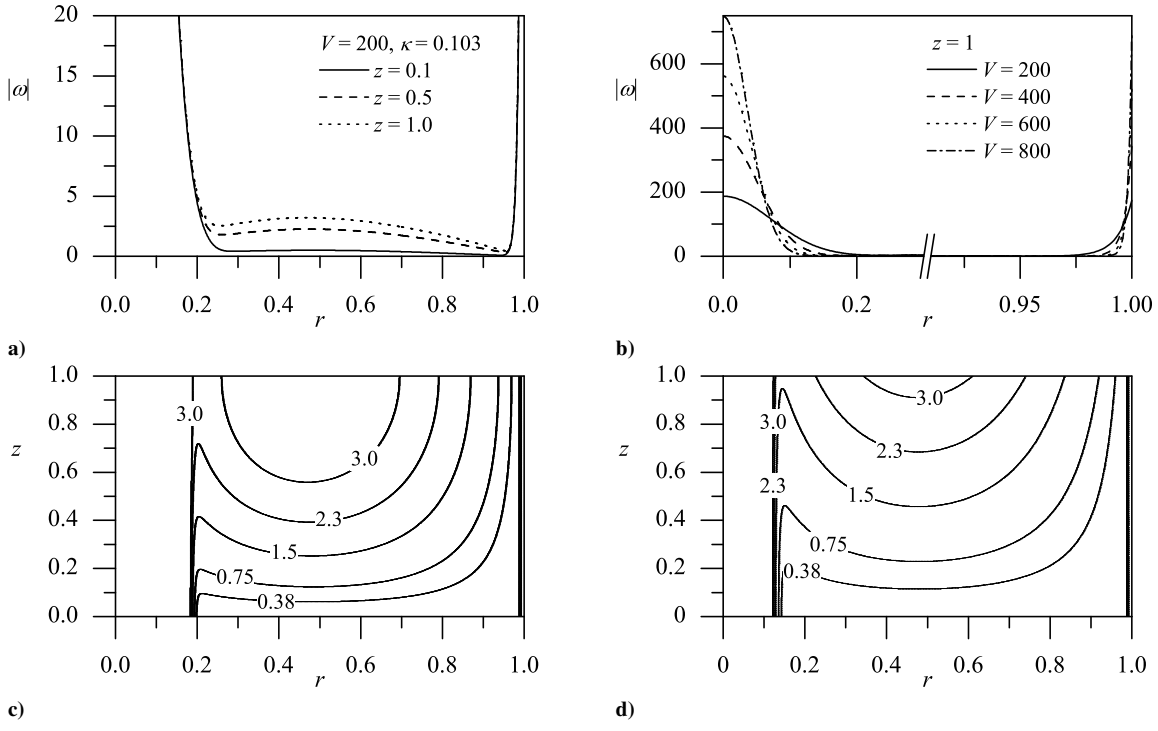

Figure 7. Vorticity plots showing effects of a) axial variations and b) sequentially increasing V. Part c) graphically compares constant vorticity lines of the nonlinear Beltramian vortex with d) its linear counterpart.

To calculate the total vorticity magnitude, we take the Pythagorean sum of the vorticity vector components and write

$$|\omega| = \left\{ \frac{\kappa^2\left(-2e^{-\frac{V}{2\pi}\alpha(1-r)}Vl^2\alpha\lambda_0 J_0(\lambda_0 r) - \left(1-e^{-\frac{V}{2\pi}\alpha(1-r)}\right)\pi\left(\pi^2+4l^2{\lambda_0}^2\right)J_1(\lambda_0 r)\right)^2}{16l^2\pi^2\beta^2{J_1}^2(\lambda_0\beta)}\sin^2\left(\tfrac{1}{2}\pi z/l\right) \right.$$
$$+r^{-2}\left[\frac{V}{\pi}\gamma r e^{-\frac{V}{2\pi}\gamma r^2} - \frac{V}{2\pi}\alpha e^{-\frac{V}{2\pi}\alpha(1-r)} \right.$$
$$\left. + \frac{r\kappa^2\left(\pi^2+4l^2{\lambda_0}^2\right)\sin^2\left(\frac{1}{2}\pi z/l\right)J_1(\lambda_0 r)\left[r\lambda_0 J_0(\lambda_0 r)+2J_1(\lambda_0 r)-r\lambda_0 J_2(\lambda_0 r)\right]}{4\beta^2 J_1^2(\lambda_0\beta)\sqrt{4+\frac{r^2\kappa^2 z^2\left(\pi^2+4l^2{\lambda_0}^2\right){J_1}^2(\lambda_0 r)}{\beta^2 J_1^2(\lambda_0\beta)}\sin^2\left(\frac{1}{2}\pi z/l\right)}} \right]^2$$
$$\left. + \frac{\pi^2 r^2\kappa^4\left(\pi^2+4l^2{\lambda_0}^2\right)^2\sin^2\left(\frac{\pi z}{l}\right)J_1^4(\lambda_0 r)}{64l^2\beta^2{J_1}^2(\lambda_0\beta)\left[4\beta^2{J_1}^2(\lambda_0\beta)+r^2\kappa^2\left(\pi^2+4l^2{\lambda_0}^2\right)J_1^2(\lambda_0 r)\sin^2\left(\frac{1}{2}\pi z/l\right)\right]} \right\}^{1/2} \tag{61}$$

where higher-order terms in κ are not kept. Equation (61) is illustrated in Fig. 7 where both vorticity magnitudes and isolines are evaluated over the chamber volume. In Fig. 7a, we hold $V = 200$ and vary z to the extent of realizing that the small sensitivity in ω to the axial position stays confined to the outer, inviscid flow region. Conversely, the successive increases in the vortex Reynolds number, shown in Fig. 7b, seem to exclusively influence the boundary layer regions. Figures 7d and 7c offer comparisons between the nonlinear (left) and linear Beltramian iso-vorticity lines (right) over the chamber volume. Both models show an increase in vorticity along the length of the chamber. However, the vorticity in the nonlinear Beltramian solution displays the fastest decay near the centerline, the most longevity in the vicinity of the headwall, and the most intensity in the exit plane. The nearly vertical lines that parallel the axis of rotation and sidewall are caused by the spatially invariant thickness of the boundary layers that emerge at both ends of the domain. These lines constitute the asymptotic boundaries that bracket the predominantly inviscid, bulk fluid region.

V. Conclusions

This study constitutes the second installment devoted to the description of the confined Beltramian vortex in the context of bidirectional motion in a right-cylindrical chamber. Whereas Part 1 focuses on the axially linear motion and its fundamental properties, Part 2 seeks to characterize the flow attributes associated with the onset of a spatially nonlinear profile. In both models of helical motions, the establishment of a forced vortex core is showcased along with the development of sidewall boundary layers. These are needed to rectify the otherwise inviscid solution and overcome, in the process, the velocity's unbounded response at the centerline and slippage at the sidewall. In so doing, we arrive at a viscous-augmented profile that can be used to more realistically model the flowfield in the bidirectional vortex chamber.

By employing the inviscid model as the far-field solution, we are able to introduce stretched coordinates and rescale the core and wall regions to the extent of identifying the inner boundary layer equations that control these viscous-dominated domains. A dependent-variable transformation is then utilized to convert the far-field condition on the inner solution from a spatially-dependent function into a manageable constant. Unlike the complex-lamellar or linear Beltramian analyses, an additional transformation is required to spatially average the sinusoidally varying radial velocity prior to its substitution into the inner boundary layer equations. These various transformations are necessary to obtain uniformly valid approximations in all three directions.

Given the three matched-asymptotic solutions at hand, their boundary layer thicknesses are easily extracted and characterized. We find the linear and nonlinear Beltramian solutions to possess nearly identical boundary layers that are prescribed by the spiraling tangential layer with nearly constant thickness. Both models exhibit faster motions and thinner viscous regions than their complex-lamellar predecessor. As one would expect, they all display a strong dependence on the vortex Reynolds number and a weak dependence on the axial position, except for their axial velocity and vorticity that remain sensitive to the axial location.

In evaluating the pressure gradient, all axial dependence is found to be inconsequential. This is especially true in the nonlinear Beltramian case where the axial coordinate remains bracketed by the sine function over the interval $0 \le z \le l$. This feature results in a simpler expression for the radial pressure gradient and corresponding pressure distribution than that in the linear case. The remaining pressure terms stem from the overarching tangential velocity and may be seen to resemble those of the complex-lamellar solution. Physically, terms connected with the axial and

radial velocities tend to be of order κ^2 and, hence, negligible. In the same vein, the pressure produced from the axial gradient is found to be sufficiently small to warrant its dismissal.

As for the vorticity distribution, it bears a striking resemblance to its linear Beltramian counterpart. Iso-vorticity lines in the present situation persist much farther upstream and exhibit higher values at any axial station. However, they seem to decay slightly more rapidly as the centerline is approached. These trends suggest that the onset of turbulence may appear sooner in the nonlinear Beltramian vortex as the Reynolds number is increased. Conversely, the inviscid region appears to be the widest for this model.

In closing, it may be useful to remark that the Beltramian profiles stand to offer reasonable approximations to describe slightly dissimilar cyclonic motions in confined cylindrical chambers. A similar mathematical framework may be used to obtain formulations for external Beltramian motions in unbounded domains. At this point, further investigations will be necessary to test the validity of the present academic solutions through numerical simulations and laboratory experiments. The ability to incorporate arbitrary injection profiles will also be desirable. These as well as other lines of research inquiry are hoped to be addressed in forthcoming work.

Acknowledgments

This project was completed with support from the National Science Foundation through Grant No. CMMI-0928762, Dr. Eduardo A. Misawa, Program Director.

References

[1]Gloyer, P. W., Knuth, W. H., and Goodman, J., "Overview of Initial Research into the Effects of Strong Vortex Flow on Hybrid Rocket Combustion and Performance," *CSTAR Fifth Annual Symposium*, Paper N96-16953, Tullahoma, Tennessee, Jan. 1993.

[2]Knuth, W., Chiaverini, M., Sauer, J., and Gramer, D., "Solid-Fuel Regression Rate Behavior of Vortex Hybrid Rocket Engines," *Journal of Propulsion and Power*, Vol. 18, No. 3, 2002, pp. 600–609. doi:10.2514/2.5974.

[3]Chiaverini, M., Malecki, M., Sauer, J., Knuth, W., and Majdalani, J., "Vortex Thrust Chamber Testing and Analysis for O2-H2 Propulsion Applications," *39th AIAA/ASME/SAE/ASEE Joint Propulsion Conference and Exhibit*, AIAA Paper 2003-4473, Huntsville, Alabama, July 2003.

[4]Matveev, I., and Serbin, S., "Modeling of the Coal Gasification Processes in a Hybrid Plasma Torch," *IEEE Transactions on Plasma*, Vol. 35, No. 6, Dec. 2007, pp. 1639–1647. doi:10.1109/TPS.2007.910134.

[5]Matveev, I., Matveeva, S., and Serbin, S., "Design and Preliminary Test Results of the Plasma Assisted Tornado Combustor," *43rd AIAA Joint Propulsion Conference and Exhibit*, AIAA Paper 2007-5628, Cincinnati, Ohio, July 2007.

[6]Matveev, I., Matveeva, S., Kirchuk, E., and Serbin, S., "Experimental and Theoretical Investigations of a Triple Vortex Combustor with Spatial Arc," *46th AIAA Aerospace Sciences Meeting and Exhibit*, AIAA Paper 2008-963, Reno, Nevada, Jan. 2008.

[7]Fang, D., Majdalani, J., and Chiaverini, M. J., "Simulation of the Cold-Wall Swirl Driven Combustion Chamber," *39th AIAA/ASME/SAE/ASEE Joint Propulsion Conference*, AIAA Paper 2003-5055, Huntsville, AL, July 2003.

[8]Fang, D., Majdalani, J., and Chiaverini, M. J., "Hot Flow Model of the Vortex Cold Wall Liquid Rocket," *40th AIAA/ASME/SAE/ASEE Joint Propulsion Conference*, AIAA Paper 2004-3676, Fort Lauderdale, FL, July 2004.

[9]Vyas, A., and Majdalani, J., "Exact Solution of the Bidirectional Vortex," *AIAA Journal*, Vol. 44, No. 10, 2006, pp. 2208. doi:10.2514/1.14872.

[10]Majdalani, J., and Rienstra, S., "On the Bidirectional Vortex and Other Similarity Solutions in Spherical Coordinates," *Journal of Applied Mathematics and Physics (ZAMP)*, Vol. 58, No. 2, 2007, pp. 289–308. doi:10.1007/s00033-006-5058-y.

[11]Sullivan, R., "A Two-Cell Vortex Solution of the Navier-Stokes Equations," *Journal of Aerospace Sciences*, Vol. 26, 1959, pp. 767–768.

[12]Bloor, M., and Ingham, D., "The Flow in Industrial Cyclones," *Journal of Fluid Mechanics*, Vol. 178, 1987, pp. 507–519. doi:10.1017/S0022112087001344.

[13]Majdalani, J., and Chiaverini, M. J., "On Steady Rotational Cyclonic Flows: The Viscous Bidirectional Vortex," *Physics of Fluids*, Vol. 21, No. 10, 2009, pp. 103603. doi:10.1063/1.3247186.

[14]Batterson, J. W., and Majdalani, J., "Sidewall Boundary Layers of the Bidirectional Vortex," *Journal of Propulsion and Power*, Vol. 26, No. 1, 2009, pp. 102–112. doi:10.2514/1.40442.

[15]Maicke, B. A., and Majdalani, J., "A Constant Shear Stress Core Flow Model of the Bidirectional Vortex," *Proceedings of the Royal Society of London. Series A*, Vol. 465, No. 2103, 2009, pp. 915–935. doi:10.1098/rspa.2008.0342.

[16]Smith, J. L., "An Experimental Study of the Vortex in the Cyclone Separator," *Journal of Basic Engineering-Transactions of the ASME*, Vol. 84, No. 4, December 1962, pp. 602–608.

[17]Smith, J., "An Analysis of the Vortex Flow in the Cyclone Separator," *Journal of Basic Engineering-Transactions of the ASME*, Vol. 84, No. 4, December 1962, pp. 609–618.

[18]Majdalani, J., "Exact Eulerian Solutions of the Cylindrical Bidirectional Vortex," *45th AIAA/ASME/SAE/ASEE Joint Propulsion Conference and Exhibit*, AIAA Paper 2009-5307, Denver, Colorado, Aug. 2009.

[19]Prandtl, L., "Zur Berechnung der Grenzschichten," *Zeitschrift für angewandte Mathematik und Mechanik (ZAMM)*, Vol. 18, No. 1, 1938, pp. 77–82. doi:10.1002/zamm.19380180111.

[20]Batterson, J. W., and Majdalani, J., "On the Viscous Bidirectional Vortex. Part 1: Linear Beltramian Motion," *46th AIAA/ASME/SAE/ASEE Joint Propulsion Conference and Exhibit*, AIAA Paper 2010-6763, Nashville, Tennessee, July 2010.

[21]Culick, F. E. C., "Rotational Axisymmetric Mean Flow and Damping of Acoustic Waves in a Solid Propellant Rocket," *AIAA Journal*, Vol. 4, No. 8, 1966, pp. 1462–1464. doi:10.2514/3.3709.

[22]Morgan, A., "Possible Similarity Solutions of the Laminar, Incompressible, Boundary Layer Equations," *Transactions of the American Society of Mechanical Engineers*, Vol. 80, 1958, pp. 1559.

[23]Morgan, A., "The Reduction by One of the Number of Independent Variables in some Systems of Partial Differential Equations," *The Quarterly Journal of Mathematics*, Vol. 3, No. 1, 1952, pp. 250–259. doi:10.1093/qmath/3.1.250.

[24]Blasius, H., "Grenzschichten in Flüssigkeiten mit Kleiner Reibung," *Zeitschrift für Angewandte Mathematik und Physik (ZAMP)*, Vol. 56, 1908, pp. 1–37.